Original

Prohaska, T.; Irrgeher, J.; Zitek, A.:

Simultaneous multi-element and isotope ratio imaging of fish otoliths by laser ablation split stream ICP-MS/MC ICP-MS

In: Journal of Analytical Atomic Spectrometry (2016) Royal Society of Chemistry

DOI: 10.1039/C6JA00087H

JAAS

PAPER

View Article Online
View Journal | View Issue

Cite this: *J. Anal. At. Spectrom.*, 2016, **31**, 1612

Simultaneous multi-element and isotope ratio imaging of fish otoliths by laser ablation split stream ICP-MS/MC ICP-MS

T. Prohaska,* J. Irrgeher† and A. Zitek

The simultaneous retrieval of spatially resolved information on the elemental content and isotope ratios from the same sampling spot (*e.g.* in incrementally grown biological material) still represents an analytical challenge. In order to assess multi-elemental (Sr/Ca; Mg/Ca; Ba/Ca; Na/Ca) and isotopic ($^{87}Sr/^{86}Sr$) data simultaneously on a fish otolith surface, a laser ablation (LA) system was coupled simultaneously to a multicollector inductively coupled plasma mass spectrometer (MC ICP-MS) and a quadrupole (single collector) ICP-MS *via* an aerosol split. In addition, a membrane desolvation nebulizer was used for introducing liquid standards in-line to the MC ICP-MS system. The recorded time resolved data of different data density (number of data points/time unit were by a factor of 4 higher using MC ICP-MS) were spatially referenced to the picture using ArcGIS® software. This allowed for the creation of elemental and isotopic images and the combination of data of different spatial resolution. Finally, regions of similar chemical composition were retrieved by cluster analysis. The method was applied to analyze an otolith of a lenok (*Brachymystax lenok*) caught in the river Eg (northern Mongolia) to assess habitat use and migration in a river system, where only little is known about the migrations of native fish. The combined statistical evaluations of the data showed that the Sr/Ca elemental and $^{87}Sr/^{86}Sr$ isotope ratios assessed in the otolith were the main discriminators of three clearly different zones on the otolith, indicating habitat shifts. Split-stream LA-ICP-MS/MC ICP-MS proved to be a compelling approach to gain elemental and isotopic data simultaneously from the same sampling spots on solid samples with a minimum loss of information.

Received 9th March 2016
Accepted 8th June 2016

DOI: 10.1039/c6ja00087h

www.rsc.org/jaas

Introduction

The chemical information stored in very small entities, such as single particles, distinct zones in geological material or biological tissues, fluid inclusions or definite layers in incrementally grown material is a very valuable source of different chemical information. Retrieving various types of chemical information from the same sampling spot on a target material by laser ablation ICP-MS still represents an analytical challenge. One major interest lies in the assessment of elemental and isotopic data simultaneously from material ablated from the identical sample compartment with maximum accuracy.

In particular, the simultaneous detection of Sr isotope ratios and trace metal levels in incrementally grown biological samples is of paramount interest[1–3] *e.g.* in fish otolith studies[4,5] where LA-ICP-MS has been established as an integral technology.[1,3,5] Until now, spatially resolved information on elemental and isotopic distributions from otoliths is typically retrieved in two separate analytical steps by retrieving the elemental information first followed by the analysis of $^{87}Sr/^{86}Sr$ isotope ratios.[5] However, LA-ICP-MS sampling destroys the sampled areas to a certain extent,[6] why usually not the same sampling spots can be analyzed by sequential ICP-MS and MC ICP-MS. Hence, in the past, different analytical approaches had to be combined to retrieve elemental and isotopic information from the same sampling spot, *e.g.* by using quasi non-destructive methods such scanning proton microprobes[7] or (synchrotron) XRF[6] for the determination of elemental distributions followed by an analysis of isotope ratios by *e.g.* LA-MC ICP-MS.[7] Also secondary ion mass spectrometry (SIMS) has been used in combination with ion microprobes for a combined monitoring of elemental and isotopic data in otoliths.[8] In some cases, LA-ICP-MS for the spatially resolved analysis of the elemental distributions were linked to the non-spatial analysis of Sr isotopes using thermal ionization mass spectrometry (TIMS).[9] However, LA-ICP-MS has been recognized as extremely versatile technique characterized by a large dynamic range (from pg g^{-1} to mg g^{-1}) and the ability for creating elemental and isotopic distribution images from the μm to mm scale.[3] Multi-element

University of Natural Resources and Life Sciences, Vienna, Department of Chemistry, Division of Analytical Chemistry, VIRIS Laboratory for Analytical Ecogeochemistry, Konrad-Lorenz-Straße 24, 3430 Tulln, Austria. E-mail: thomas.prohaska@boku.ac.at

† Currently at the Helmholtz-Centre for Materials and Coastal Research, Institute for Coastal Research Geesthacht, Department for Marine Bioanalytical Chemistry, Max-Planck-Straße 1, 21502 Geesthacht, Germany.

trace and isotope ratio analysis by laser ablation mass spectrometry typically requires two different types of MS instruments: scanning single collector ICP-MS and static multicollector ICP-MS. One approach which has been applied in the past to gather Ba/Ca, Sr/Ca ratios and $^{87}Sr/^{86}Sr$ isotope ratios in a quasi-simultaneous way, was to cycle the monitoring of different isotopes (^{83}Kr, ^{84}Sr, ^{85}Rb, ^{86}Sr, ^{87}Sr, and ^{88}Sr for 3 s and ^{48}Ca and ^{138}Ba for 1 s each) on a MC ICP-MS to retrieve quasi-simultaneous information for a specific region.[10,11] However, simultaneity of information between sampling spots is lost during this approach (compromising the spatial resolution as well as the isotope ratio precision) and the number of elements to be monitored is limited, as well.

As a consequence of the destructive nature of laser ablation, the laser leads to the inevitable loss of sample from a distinct spot after the analysis.[6] This has been recognized as limitation in comparison to electron beam, PIXE and SIMS methods.[3] *E.g.* in fish otolith analysis, the core of a fish otolith contains specific information of the earliest life stage of a fish and is usually very small in diameter, typically ranging between 30 μm and 250 μm.[12–14] This area is normally destructed after a single laser ablation event (see an image *e.g.* after a line scan through an otolith core of a typical freshwater species, the brown trout *Salmo trutta* f.f., in ref. 12) as it is also restricted in depth. Thus, multiple laser lines (or spots) are not possible on the exact same area.

A logical consequence to overcome the described limitations is the simultaneous coupling of different types of ICP-MS instruments, what has recently been accomplished in a few (mainly geological) studies. Yuan *et al.*, 2008 were one of the first to couple two ICP-MS instruments to one single laser ablation stream for the analysis of zircons.[15] Kylander-Clark *et al.* used laser ablation split stream (LASS) analysis for petro chronological investigations by coupling a multicollector and a single collector inductively coupled plasma mass spectrometer to one laser ablation system.[16] A similar coupling was presented by Fisher *et al.*, who described a setup using a laser ablation system coupled to a single collector (for U–Pb age determination) and a multicollector (for Hf isotope analyses) ICP-MS for the analysis of zones zircons.[17] Simultaneous *in situ* measurement of Rb–Sr/Sm–Nd or Sm–Nd/Lu–Hf isotopes in natural minerals using laser ablation multicollector ICP-MS was performed by Huang *et al.*[18] The authors coupled a 193 nm excimer laser ablation system to a Thermo Fisher Scientific Neptune for Sr (or Nd) analyses and a Thermo Fisher Scientific Neptune Plus for Nd (or Hf) analyses on apatite and loparite. Experiments showed that the different proportions of the ablated material for the Neptune and Neptune Plus MC ICP-MS (3 : 7, 5 : 5 and 7 : 3) did not show any significant bias for the Sr–Nd isotopes within analytical uncertainties. Goudie *et al.* performed simultaneous *in situ* determination of U–Pb and Sm–Nd isotopes in monazite by laser ablation ICP-MS, where an ICP-SFMS (for measuring U–Pb isotopes) and a MC ICP-MS (for measuring Sm–Nd isotopes) were used after the split stream.[19] Finally, Wehe *et al.* combined rapid cell (CRC) mode switching and dual laser ablation inductively coupled plasma mass spectrometry for elemental bioimaging.[20] While the first approaches simultaneously utilize two inductively coupled plasma mass spectrometers coupled to one laser ablation (LA) system, the latter study is based on a single ICP-MS instrument with fast cell mode switching (CMS) of the CRC between individual line scans. More recently, Hacker *et al.* 2015 monitored monazite response to ultrahigh-pressure subduction from U–Pb dating by laser ablation split stream.[21] Viete *et al.* 2015 (ref. 22) applied single-shot laser ablation split stream (SS-LASS) petrochronology to decipher multiple, short-duration metamorphic events *via* U/Th–Pb measurements and trace-element analyses. Aramendia *et al.*[23] directly analysed dried blood spots by femtosecond-laser ablation inductively coupled plasma mass spectrometry for Cu isotopic analysis and simultaneous multi-element analysis.

Asides the assessment of elemental and isotopic data from the same sampling spot, combined chemical imaging of data with different spatial arrangement and resolution still poses a remaining challenge.[24] Therefore, the use of geographical information systems software like ArcGIS® has been suggested by ref. 24 for an improved spatial data reduction and integration and has *e.g.* successfully been applied and published recently by ref. 25. In this work, the further development and application of imaging laser ablation split stream ICP-MS/MC ICP-MS is presented for the analysis of the elemental and Sr isotopic distributions in a fish otolith sample for the first time. The presented setup was set up independently of the previously published versions taking into account that different instruments were used and a desolvation nebulizing system was applied in addition. ArcGIS® was used as technology for spatial data integration and reduction and image creation for the first time with this setup for exact referencing of data spots from different instrumentation to the actual ablation site.

Experimental

Otolith samples and preparation

An otolith sample was prepared from a lenok (length: 382 mm, weight: 447 g (full), 399 g (empty – after evisceration)), which was caught in the river Eg, Mongolia (at N 49.44371, E 103.48368) in October 2014. One in-house reference otolith sample (named CO-288) of a brown trout with a measured homogeneous elemental and isotopic distribution (note: the fish did not show a habitat shift and different cross line sections did not show a significant variation) was used to monitor the effect of the sample split measurements on the signal and the final elemental and isotopic ratios with respect to accuracy, sensitivity and uncertainty. Otolith preparation followed standard protocols described in ref. 26. The otolith was cleaned with reagent grade I water and air-dried on a dark clean room towel before being mounted on a microscopic glass slide using Krazy Glue (Instant Krazy Glue Pen, Elmer's Products (Distributor), Westerville, Ohio, USA). After 24 h of hardening, the otolith was ground to the plane to expose the earliest otolith growth zone, the otolith core, using 30 μm and 3 μm lapping films. Finally, the otolith was rinsed with reagent grade I water, air-dried under a laminar hood and was stored in a plastic bag until analysis.

The FEBS-1 otolith certified reference material for trace elements (National Research Council of Canada, Ottawa, CA) (Table 1) was used for validation of the Sr isotope ratio measurements and for quantification. The material consists of fine otolith powder, which was pressed into a pellet by a high-pressure press (10 tons per cm^2) without using any additional binding material.

ICP-MS measurements

All laser ablation measurements were accomplished using a split stream system by connecting a laser ablation system (NWR193, Electro Scientific Industries, Portland, USA) to an ICP-QMS (NexION 350D, PerkinElmer, Waltham, USA) and a MC ICP-MS (Nu Plasma HR, Nu Instruments Ltd, Wrexham, UK). A membrane desolvation nebulizer (DSN 100, Nu Instruments Ltd, Wrexham, UK) was coupled to the line from the laser to the MC ICP-MS *via* a Y-piece connector prior to injection into the plasma in order to allow for both signal optimization of the MC ICP-MS and external intra-elemental correction for instrumental isotopic fractionation (IIF) of the obtained Sr isotope ratios (see the analytical setup in Fig. 1).

A solution of NIST SRM 987 ($SrCO_3$ certified for its Sr isotopic composition; NIST, Gaithersburg, USA), with a mass fraction of approximately 20 ng g^{-1} was introduced *via* the DSN 100 for optimization and IIF correction (at the beginning and end of each laser ablation event) *via* standard – sample – bracketing. A dried (humid) aerosol of HNO_3 (double subboiled from p.a. grade, Merck KGaA, Darmstadt, Germany) (2% w/w) obtained from double subboiled concentrated HNO_3 diluted with subboiled water was aspirated during laser ablation to maintain stable conditions. Reagent grade I water (18 MΩ cm) obtained from a purification system (ELGA Purelab, ELGA LabWater, High Wycombe, UK) was further purified by sub-boiling distillation (Savillex DST-100, AHF Analysentechnik, Tübingen, Germany). Concentrated nitric acid (p.a. grade, Merck KGaA, Darmstadt, Germany) was subjected to two sub-boiling distillation steps (Savillex DST-100) before use. Instrumental parameters are listed in Table 2.

Data reduction

All measured data were corrected for blank by subtracting the average gas blank values collected over a period of 4 minutes prior to each analysis cycle. Elemental intensity ratios of the measured isotopes were converted into molar ratios by applying the correction factor/response factor obtained by laser ablation measurements of FEBS-1. Elemental ratios were calculated taking into account the time shift caused by sequential measurements of the single isotopes by interpolation. Sr isotope ratios were calculated as point-by-point ratios of the signal intensities measured by MC ICP-MS after blank subtraction (using the on-peak zero approach provided by the Nu software) and Rb correction. Rb correction was accomplished by calculating ^{87}Rb *via* ^{85}Rb using the natural isotopic abundances and applying the mass fractionation factor calculated from the $^{88}Sr/^{86}Sr$ ratio (Russell law for IIF correction).

IIF correction of the $^{87}Sr/^{86}Sr$ ratio was accomplished by using external intra-elemental IIF correction (standard sample bracketing) measuring NIST SRM 987 introduced *via* the DSN before and after each sample (comment: internal IIF correction using $^{88}Sr/^{86}Sr$ was tested for FEBS-1 and did not lead to a significant difference in the obtained $^{87}Sr/^{86}Sr$ ratio. Nonetheless, since the $^{88}Sr/^{86}Sr$ ratio is not necessarily constant in nature, the bracketing method was considered the more versatile approach). Preparation defects like grinding and cracks or irregular otolith growth are factors that lead to measurement artefacts. These areas and data were excluded by visual inspection of the microscopic images as well as by applying an analytical threshold where the ^{43}Ca signal in the ICP-QMS measurement was below 10% of the average ^{43}Ca signal analyzed over the entire otolith surface.

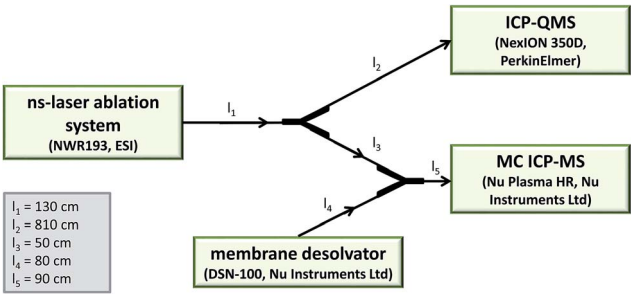

Fig. 1 Schematic diagram of LA system coupled to MC ICP-MS and ICP-QMS for simultaneous measurement of Sr isotope ratios and selected elements.

Spatial data referencing and statistical analysis

The spatial parameters of the data points are listed in Table 3. Microscope images of the grinded otolith were taken before and

Table 1 Elemental mass fractions and molar ratios in FEBS-1 (NRC, Ottawa, CA)

	Ba	Mg	Na	Sr	Pb	Ca
Elemental content/mg kg^{-1}	5.09	23.6	2594	2055	0.40–0.77 (information value)	38 300
U_{CRM} ($k = 2$)/mg kg^{-1}	0.23	1.3	161	79		1400

	Ba/Ca	Mg/Ca	Na/Ca	Sr/Ca	Pb/Ca
Molar ratio	3.88×10^{-5}	1.02×10^{-3}	1.18×10^{-1}	2.45×10^{-2}	2.02×10^{-6}

Table 2 Instrumental parameters

Laser	NWR193 (ESI)
Spot size	150 μm
Scan speed	5 μm s^{-1}
Repetition rate	20 Hz
Energy	90%
Fluence	11.68 J cm^{-2}
Irradiance	2.34 GW cm^{-2}
Carrier gas	He
Carrier gas flow rate	0.9 L min^{-1}
MC ICP-MS	Nu Plasma HR (Nu Instruments Ltd)
Axial mass	86
Mass separation	0.5
Measured isotopes	^{82}Kr, ^{83}Kr, ^{84}(Sr + Kr), ^{85}Rb, ^{86}(Sr + Kr), ^{87}(Sr + Rb), ^{88}Sr
RF power	1500 W
Auxiliary gas flow (Ar)	0.91 L min^{-1}
Plasma gas flow (Ar)	13.0 L min^{-1}
Laser carrier gas split flow (He)	0.3 L min^{-1}
HV1	4001 V
HV2	2610 V
Membrane desolvation nebulizer	DSN-100 (Nu Instruments Ltd)
Nebulizer gas pressure	32.5 psi
Hot gas flow (Ar)	0.41 L min^{-1}
Membrane gas flow (Ar)	3.58 L min^{-1}
Spray chamber temperature	112 °C
Membrane temperature	114 °C
ICP-QMS	NexION 350D (PerkinElmer)
Measured isotopes	^{13}C, ^{23}Na, ^{24}Mg, ^{43}Ca, ^{88}Sr, ^{138}Ba, ^{208}Pb
RF power	1500 W
Auxiliary gas flow (Ar)	1.25 L min^{-1}
Plasma gas flow (Ar)	18.0 L min^{-1}
Laser carrier gas split flow (He)	0.61 L min^{-1}
Laser additional gas flow (Ar)	1.00 L min^{-1}

Table 3 Spatial parameters of the data points

Parameter	Nu Plasma HR (Sr isotope ratios)	Nexion 350D (elemental ratios)
Integration time/s	0.20	0.050
Time span between data points/s	0.20	0.402
Length per data point/μm	1.00	2.01
Data points per spot size	150	74.6

after the laser ablation including a spatial scale into the image. In a next step, the image was referenced in ArcGIS® (ArcMap 10.2.1. ESRI, Redlands, California) by using this spatial reference scale. This step created the spatial reference system for the image. The laser lines were digitized and the *x*–*y* coordinates of starting and end point of lines were determined. Hereby the starting points were set half a spot size away from the line start, as each data point reflects the center of an area determined by the spot size. These data were exported from ArcGIS® and imported into Microsoft® Excel where the coordinates between the start and endpoint were calculated for each data point of the time resolved line scans.[25] The line scan data equipped with *x*–*y* coordinates were re-imported into ArcGIS® and displayed as a direct overlay of the otolith image. In consecutive steps outlier detection, 3-D visualisation and data integration were performed directly in ArcGIS®. First, the outliers of the elemental and Sr isotope dataset were identified and removed using the *Cluster and Outlier Analysis* (Anselin Local Moran's *I*) of ArcGIS®[27,28] with a spatial range of twice the spot size (300 μm). This tool is able to identify concentrations of high values, concentrations of low values, and spatial outliers given a set of features (input feature class = all laser spots as a point layer) and an analysis field (input field = *e.g.* Sr isotope ratio). To do this, a local Moran's *I* value, a *z*-score and a *p*-value are calculated and a code representing the cluster type for each statistically significant feature is created. A positive value for *I* hereby indicates that a data point has neighboring data points with similarly high or low values for the selected attribute, considering the data point as element of a cluster. In contrast, a negative value for *I* indicates that a data point has neighbors with very different values, making it prone to be an outlier. In both cases, either for the cluster or the outlier, the *p*-value for the data point has to be small enough to be considered as statistically significant. In our case the statistical significance was set at the 95 percent confidence level.

The cluster/outlier type is automatically displayed after the calculation in a separate column in the ArcGIS data file for each data point, distinguishing between statistically significant clusters of high values (HH), clusters of low values (LL), an outlier with a high value surrounded primarily by low values (HL), and an outlier with a low value surrounded primarily by high values (LH).

In a next step a stacked 3D image of all data points of the Sr/Ca ratio and the ^{87}Sr/^{86}Sr isotope ratio was produced for visualizing regional patterns of both parameters (ArcScene 10.2.1. ESRI, Redlands, California).

To improve the visual interpretability of the 3D visualization, the coloration of data points was set by classes based on natural groupings ('natural breaks' or 'natural jenks') inherent in the data.

Hereby ArcGIS automatically sets break points by selecting the class breaks that best group similar values while maximizing the differences between classes. The ^{87}Sr/^{86}Sr data that were gathered in higher spatial density by MC ICP-MS than element/Ca ratios by Q ICP-MS were averaged according to the spatial resolution of the elemental data gathered at lower spatial resolution in *x*-direction as a result of the longer total integration time. Therefore, the elemental data were buffered according to their spot size (150 μm) in ArcGIS® first. The Sr isotope data were attached with a spatial join to the elemental data areas (with a diameter of 150 μm) and their average, standard deviation and variance values were calculated. On average each elemental data point – reflected as area representing a spot size of 150 μm – contained 152 Sr isotope ratio data points. The data of one cross sectional line was displayed as stacked Microsoft® Excel figure (Fig. 2) to demonstrate the

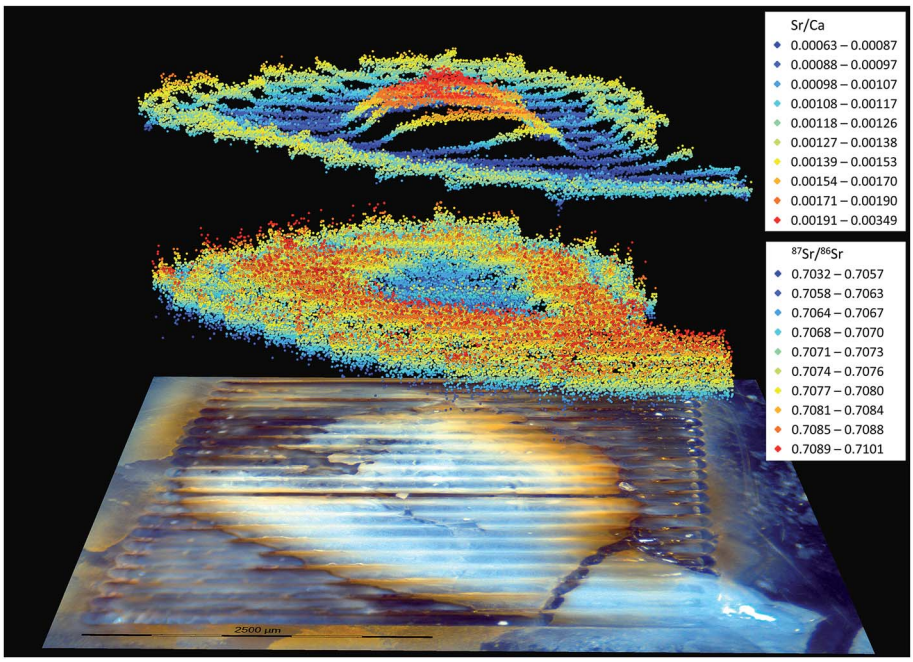

Fig. 2 3D visualization of the spatially referenced data of the Sr/Ca elemental ratio (upper layer) and $^{87}Sr/^{86}Sr$ isotope ratio (lower layer) combined with a microscope image of the investigated otolith sample after laser ablation (note the different density of data points and the clearly visible zonation of regions, with transition zones created when moving from higher Sr/Ca elemental ratios to lower ratios (upper image)).

combined fluctuations of Sr/Ca values in relation to the original $^{87}Sr/^{86}Sr$ isotope ratio data and the averaged $^{87}Sr/^{86}Sr$ isotope ratio data, respectively.

To visualize the 'true' spatial resolution of the data points, chemical images showing the data points buffered by the spot diameter were produced. Cluster analysis was chosen as chemometric tool[25] to identify specific regions on the whole otolith surface with significantly different chemical information. The joined data containing the element/Ca ratios and $^{87}Sr/^{86}Sr$ ratios were exported to a dbf-file and imported into IBM SPSS 21.0 (IBM SPSS Statistics for Windows, Version 21.0. Armonk, NY: IBM Corp) for statistical data evaluation.

Cluster analysis was performed using the *TwoStep Cluster Analysis* of IBM SPSS with *log-likelihood* as distance measure and automatic determination of the number of clusters. The *Two-Step Cluster Analysis*, in comparison to traditional clustering methods, is able to deal with very large datasets (like in our case the high number of data points) and the automatic determination of the number of clusters at the same time.[29] In the first step a pre-clustering is performed and in step 2 the sub-clusters resulting from the first step are used as input. These values are then grouped into an automatically defined optimized number of clusters.

Data were standardized before analysis and a cluster membership variable was determined. Mean values, standard deviations and boxplots for all parameters of each cluster were calculated. Finally, all data including the cluster assignments to each data point were saved as .xlsx file and re-imported into ArcGIS, where the clusters were displayed as zones on the otolith.

Results

The parameters, which were used to study the effect of the split stream on instrumental performances by ablating the reference otolith CO-288 are summarized for Sr in Table 4. The sensitivity of NIST SRM 987 solution aspirated *via* the DSN did not show significant difference when changing to the split stream setup. Therefore, no significant change in sensitivity of the MC ICP-MS setup was observed. The reduction of the laser ablation signal intensity during split stream laser ablation in the MC ICP-MS and the ICP-QMS is therefore the direct result of the split stream and the reduced amount of material, which is transported to each MS. The measurement precision (calculated as 2 × SD of a single line of 100 µm length) and the uncertainty of the Sr isotopic composition was not affected by the split stream, either. The LOD and the RSD of element/Ca ratios are given in Table 5.

The wash-in time calculated from the change of the blank signal from >3 × SD of the gas blank signal until a plateau was reached (indicated by the average signal at the plateau) did increase by factors of about 1.75 and 1.65 for the Nu Plasma and NexIon respectively. The wash-out time represents the time from the average plateau signal until a signal lower than the signal precision was reached. The wash-out time did not increase significantly for the Nu Plasma, but did increase by a factor of 1.2 for the NexIon. This can be explained by the increased length of the transfer line length (8 m) from the laser to the NexIon compared to a 50 cm transfer line from the laser to the Nu Plasma. This effect was further taken into account by reducing the scan speed to 5 µm s^{-1}. The relative time delay of

Table 4 Instrument behavior without and with split stream (SSLA)

	Sample	Nu Plasma HR LA-ICP-MS	Nu Plasma HR SSLA-ICP-MS	NexION LA-ICP-MS	NexION SSLA-ICP-MS
Signal intensity (total Sr)	CO-288	23.4 V	5.86 V	2.3×10^6 cps	1.2×10^6 cps
	NIST SRM 987@20 ng g^{-1} (DSN)	2.6 V	2.3 V	✗	✗
$\Delta^{87}Sr/^{86}Sr$[a]	CO-288	0.0 per mil	−1.38 per mil	✗	✗
$\Delta^{87}Sr/^{86}Sr$[a]	NIST SRM 987	0.0 per mil	−1.40 per mil	✗	✗
IIF factor	NIST SRM 987	−1.53	−1.69	✗	✗
u_c ($^{87}Sr/^{86}Sr$) (split stream laser ablation data)[b]	CO-288	0.025%	0.025%	✗	✗
u_c ($^{87}Sr/^{86}Sr$) (split stream liquid nebulization data)[b]	NIST SRM 987	0.006%	0.009%	✗	✗
Sr/Ca precision ($n = 100$)	CO-288	✗	✗	4.8%	5.0%
Wash-in	CO-288	0.8 s	1.4 s	0.9 s	1.5 s
Wash-out (long line, NexIon)	CO-288	1.8 s	1.9 s	2.8 s	3.5 s
Wash-out (short line, Nexion)	CO-288	✗	✗	1.7 s	✗
Gas blank ^{88}Sr	Gas blank	−0.0022 V	−0.0023 V	0–4.0 cps	0–4.0 cps

[a] Raw intensities were only corrected for blank and the measured ratio of CO-288 obtained by LA-MC ICP-MS was taken as zero reference value. [b] Precision was calculated from 60 data points.

Table 5 RSD for elemental molar ratios and LOD (based on FEBS pellet LA-ICP-MS measurements)

	Ba	Mg	Na	Sr	Pb	Ca (^{43}Ca-signal)
RSD/% (element/Ca ratio; 150 μm line)	31	34	11	5.2	130	26.0
LOD/mg kg^{-1}	0.035	6.89	130	0.31	0.84	nD

the signal response between the two instruments were between 3.0 ± 0.1 seconds. This value is in good agreement with the gas flow rate through the tubing (0.6 L min^{-1}) and the length difference of the lines (see Fig. 1). The differences in the measured ratio show that the IIF in the MC ICP-MS is influenced mainly by the gas flows in the system.

According to the different integration times, measurements resulted in different densities of data points for elemental/Ca and isotope ($^{87}Sr/^{86}Sr$) ratios. The 3D visualization shows the general zonation of the otolith based on the complementary information gathered from both instruments only for Sr/Ca (Fig. 2) whereas the other elemental/Ca ratios do not vary significantly within the otoliths. The further statistical evaluation of elemental data led also to the conclusion that only Sr shows a distinct pattern in the classification based on statistical data treatment. As a consequence, only Sr is discussed in detail in the further considerations. A selected cross sectional line through the core of the otolith further visualizes the combined fluctuations of Sr/Ca values in relation to the original $^{87}Sr/^{86}Sr$ isotope ratio data and the averaged $^{87}Sr/^{86}Sr$ isotope ratio data (Fig. 3). The central otolith area (representing the juvenile habitat) is characterized by elevated Sr/Ca ratio and a stable plateau of $^{87}Sr/^{86}Sr$ isotope ratio. A short transition zone leading to significantly lowered Sr/Ca ratios and elevated $^{87}Sr/^{86}Sr$ isotope ratios follows this region. The value in this transition decreases/increases linearly according to the transition of the laser spot between zones of different signal intensities. Finally the outer area of the otolith is characterized by intermediate fluctuating values of both parameters. Fig. 4 shows the buffered data points to visualize a most realistic representation of the spatial resolution of each data point, which is achieved by a laser spot of 150 μm in line scan mode at a scan rate of 5 μm s^{-1}.

Discussion

A laser ablation split stream ICP-MS/MC ICP-MS setup for the analysis of the elemental and isotopic distributions in a fish otolith sample was successfully developed. The instrumental difference to previously used setups is the fact that an additional desolvation nebulizing system was introduced. The additional introduction of a liquid solution was accomplished by Aramendia,[23] who used a cyclonic nebulizer instead. The advantage of a desolvation membrane is obvious since it creates stable plasma conditions but simultaneously keeps the H_2O load to the plasma low in order to avoid oxygen based interferences, which is of major concern for *e.g.* Sr isotope ratio measurements in hydroxyl apatite matrices due to the ArPO interference on mass 87. The change in wash-in and wash-out times caused by the increased tubing line length to the ICP-QMS could be corrected for. Nonetheless, the use of laser cells with faster wash-out times would be of advantage in the proposed split stream setup. In combination with increasing sensitivity of modern mass spectrometers, a further

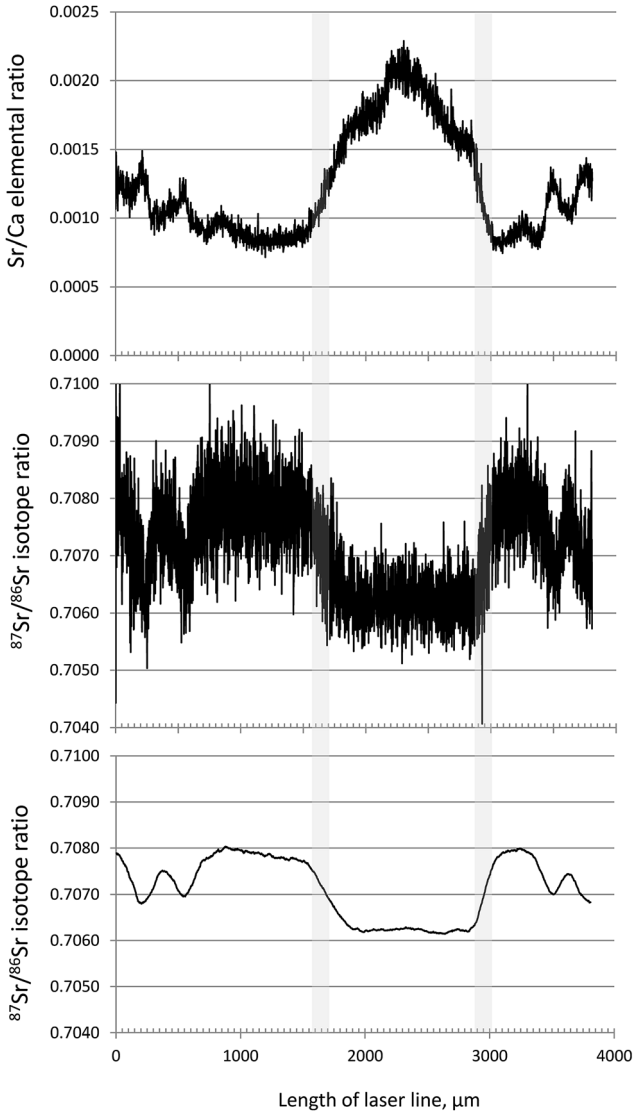

Fig. 3 LA-(MC) ICP-MS data from one selected line cross section displaying all data points for the Sr/Ca elemental ratio (upper graph), all data points for the $^{87}Sr/^{86}Sr$ isotope ratio (middle graph) and the $^{87}Sr/^{86}Sr$ isotope ratio data points integrated after buffering (lower graph) according to the applied spot size. The grey line displays the spot size and visualizes the influence of the spot size on the signal in the transition regions between high/low or low/high values.

improvement in the spatial information content can be expected since the limitation in the spatial resolution can be seen as a combination of laser spot size, scan speed and washout times. In order to enable proper interpretation of the obtained images, buffering of the data occurred to be a prerequisite to deal with differences in distance between data points, as well. Thus, downscaling of the data with higher spatial resolution as accomplished in ArcGIS® proved to represent a rather realistic picture of the actual laser ablation data. The interpretation of irregularities in the data as a result of preparation artefacts or artefacts caused by the transition of the laser over areas of significantly changing signal intensities is a prerequisite in order to avoid misinterpretation of the acquainted data by the following image interpretation using dedicated software.

In general ArcGIS as a geographical information system has the ability to integrate data points of different spatial arrangement and resolution (like laser spots in point ablation mode, or line ablations where the lines also might have irregular distances in *y* direction) without prior interpolation based on their referenced spatial position. This is in contrast to other imaging tools that are applied to create image-like representations of distributions of chemical constituents of samples and combine these representations with underlying image photographs like ImageJ. These tools require rasterized grids of pixels as input. Because interpolation is required before data can be imported in ImageJ, typically the images created based on data with different densities in *x* and *y* direction are prone to a "stretching effect" in the direction of lower information density. With some effort it is possible to add "empty" pixel rows between the pixel rows representing the ablated lines. This becomes practically impossible in cases where lines are not completely parallel. Moreover, data points created by LA-ICP-MS represent areas defined by the set spot diameter. The actual diameter might be different from the preselected value (*e.g.* influenced by the laser beam focus). The actual dimension of the laser spot can be represented in ArcGIS by buffering the data points according to their diameter retrieved from the images. Here, the creation of coordinates after the ablation process by digitizing the ablated spots or lines also helps to overcome spatial irregularities created during the ablation caused by stage drift. This is of importance especially in situations when a high spatial resolution is required (*e.g.* 10 µm spot size). Therefore the main advantages of ArcGIS are the possibility of exact referencing of data points to the actual ablation site and also adequate buffering based on the "true" laser diameter. In case of defocusing of the laser and stage drift this can be determined manually from the sample image in post-processing based on the real position and dimension of the ablated information on the sample.

As ArcGIS is able to treat each data point individually, no interpolation between point ablations and (maybe irregularly spaced) line ablations is needed before the data can be matched with underlying images. This fact improves interpretation and extraction of information from regions of interest. However, ArcGIS allows also for interpolation of data points to create continuous surfaces, but has as a targeted tool for spatial data treatment more capabilities to deal with spatial point and line data of different resolution arranged in different ways on the sample. This means, it can deal, overlay and integrate easily data from different lasering campaigns (lines, spots, diagonal measurements *etc.*) and from other sources. Only few available software packages for creating images based on transient LA-ICP-MS data offer similar capabilities. To our knowledge, only Cellspace,[30] a module used within the IOLITE software package[31] targets at the representation of laser spots as areas ("similar to buffering"). Only recently, an approach to align sampling spots of defined diameter containing measured values with images based on ImageJ to represent information on incrementally grown biological matrices like shells and

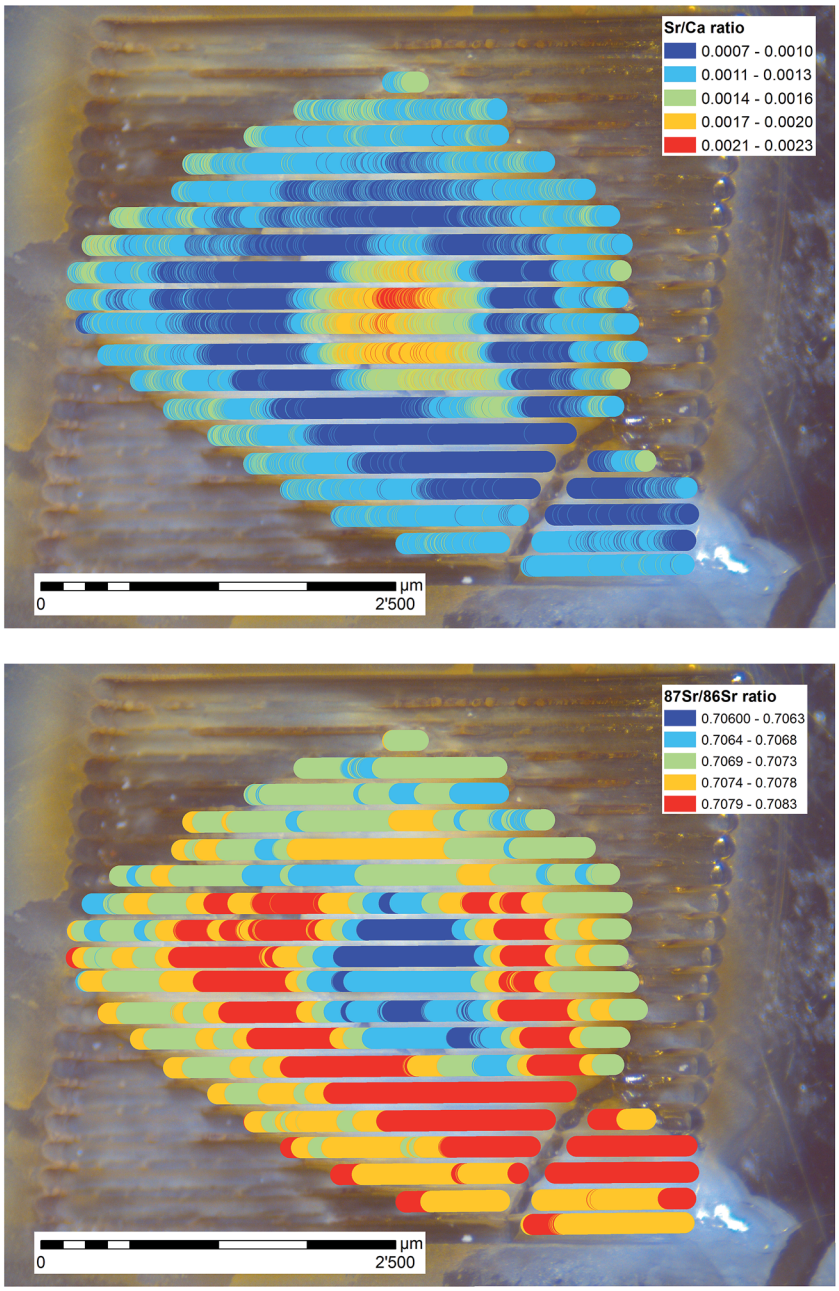

Fig. 4 Buffered data points of the Sr/Ca ratio (upper image) and the $^{87}Sr/^{86}Sr$ isotope ratio values (lower image) averaged to the 150 µm spot size and a line scan speed of 5 µm s^{-1}.

otoliths has been presented. The presented workflow is much more complicated and lacking the ability to deal with high numbers of data points and the comprehensive and powerful analytical tools ArcGIS is providing.[32] As a result, in the investigated example, the final cluster analysis of the fish otolith revealed that Sr/Ca elemental ratio and $^{87}Sr/^{86}Sr$ ratios were the main discriminators in habitat determination of the analyzed fish *via* the elemental information stored in otoliths. This effect can be expected to be typical for fresh water fish species since similar results were found in previous studies.[33] These two parameters revealed 3 clusters (Fig. 5) with significantly different and characteristic combinations (Fig. 6). The cluster situated in the center of the otolith reflects the juvenile habitat of the fish with higher Sr/Ca ratio and lower $^{87}Sr/^{86}Sr$ isotope ratios followed by a clear habitat shift after this time as described above. The transition to the adjacent cluster with lower Sr/Ca ratio and higher $^{87}Sr/^{86}Sr$ isotope ratios is characterized by linearly changing values until a new plateau represented by the outer cluster is reached. This intermediate cluster can be clearly explained by the laser shift and spot size and relates to an analytical artifact, which can be improved by using smaller spot sizes and a cell with shorter washout times. The second pronounced cluster clearly appears as a result of a habitat shift after the first living phase of the fish.

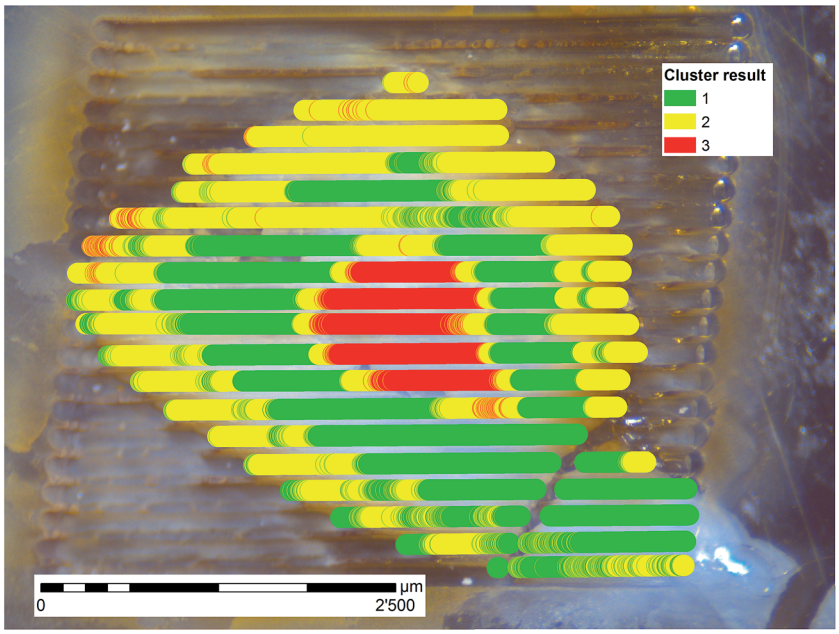

Fig. 5 Clusters gained by a cluster analysis using the Sr/Ca elemental ratio and the $^{87}Sr/^{86}Sr$ isotope ratio displaying three clusters revealing at least three clearly differing zones (excluding the transition zones between the first two central regions).

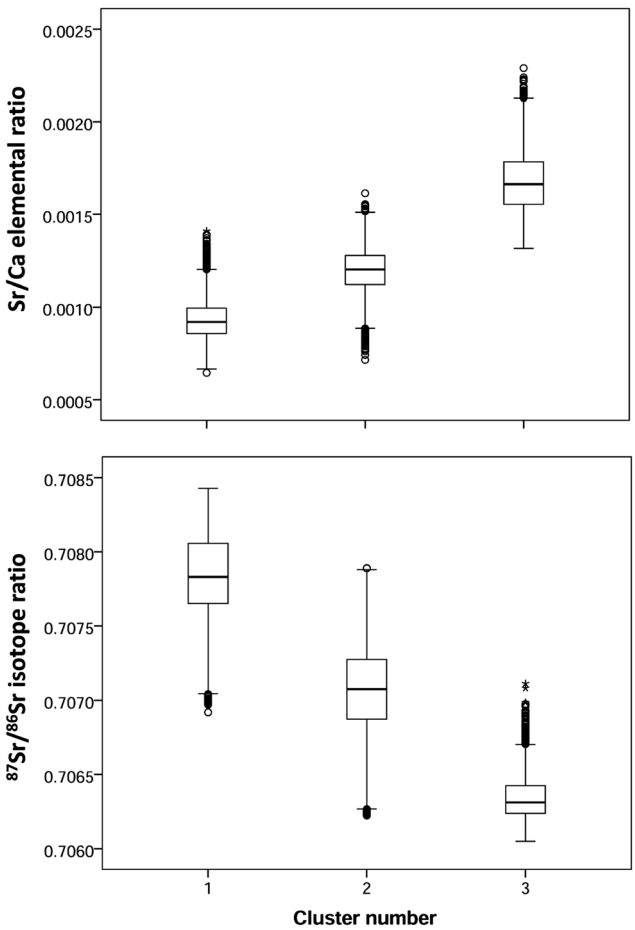

Fig. 6 Value ranges for Sr/Ca ratios (upper) and $^{87}Sr/^{86}Sr$ (lower) in the three significantly different clusters characterizing different otolith regions.

However, the outer area of the otolith is characterized by fluctuating values as displayed by the cross sectional data profiles (Fig. 3).

It is plausible that this region dispatches not only a single habitat but also a behavior characterized by migrations between the juvenile habitat and the later habitat at durations that could not be resolved by the applied system considering the otolith growth during the respective habitat use. Therefore each data point might reflect a mixed signal yielding values lying between both habitats.

Also the use of the mixture zone of both habitats *e.g.* at a river/tributary confluence is possible. It is evident that the information gained from otoliths needs to be matched with the known behavior and life cycle of the fish species under study.[34] A specific attribution of the chemical information to a specific habitat requires additional water samples and the creation of an aquatic isoscape[35] preferably with time resolution to exhibit possible seasonal fluctuations. The work of mapping the chemical composition of the water bodies is currently ongoing.

Conclusions

Imaging laser ablation split stream ICP-MS/MC ICP-MS analysis proved to be a way forward to increase the information content gained in a spatially resolved manner from solid samples as it provides elemental and isotopic data from the same sampling spots at low elemental concentration levels. Instrumental settings of both instruments and the resulting spatial arrangement of data can be best integrated using a geospatial approach, *e.g.* by using ArcGIS®, allowing also for the detection of regional outliers by spatial statistics, data reduction and joint analysis of data points retrieved from multiple instruments in

different spatial and temporal resolution. Especially in situations with irregular spatial arrangements of data spots and lines, a geospatial treatment of ablation spots as areas has significant advantages over an imaging approach requiring rasterized pixels as input. The combination of different visualization approaches and chemometric tools improves the interpretation of spatially resolved LA-ICP-MS data. It adds another important option for many applications that need to retrieve chemical data from small sampling spots requiring multiple instruments by limiting the loss of information during laser ablation and maximizing the output of information gained from one single analysis. As a consequence, the reconstruction of life histories of fish by zones determined by a combination of multiple elemental and isotopic variables in otoliths can be improved by the proposed methodological approach.

Acknowledgements

We would like to thank Olaf Jensen, Jensen lab, in the Department of Marine & Coastal Sciences at Rutgers University (The State University of New Jersey), and the Taimen Conservation Fund (TCF), Mongolia for the financial support of this work as part of the study "Assessment of Egiin Gol Hydropower Project". We also would like to thank Ganzorig Batsaikhan, Munkhzorig Battulga and Unurjargal Tsevegdorj for catching the lenok in the Eg river, and extracting the otoliths. Also the support of the work by the Food and Agricultural Organization (FAO), namely by Gerd Marmulla, Fishery Resources Officer for Inland Fisheries at the FAO Fisheries and Aquaculture Department Marine and Inland Fisheries Service (FIRF), is highly acknowledged.

References

1 S. F. Durrant and N. I. Ward, *J. Anal. At. Spectrom.*, 2005, **20**, 821–829.
2 P. Outridge, G. Veinott and R. Evans, *Environ. Rev.*, 1995, **3**, 160–170.
3 J. D. Woodhead, J. Hellstrom, J. M. Hergt, A. Greig and R. Maas, *Geostand. Geoanal. Res.*, 2007, **31**, 331–343.
4 S. E. Campana, *Mar. Ecol.: Prog. Ser.*, 1999, **188**, 263–297.
5 S. M. Turner, K. E. Limburg and E. P. Palkovacs, *Can. J. Fish. Aquat. Sci.*, 2015, **72**, 845–854.
6 K. E. Limburg, R. Huang and D. H. Bilderback, *X-Ray Spectrometry*, 2007, vol. 36, p. 336.
7 P. Outridge, S. Chenery, J. Babaluk and J. Reist, *Environ. Geol.*, 2002, **42**, 891–899.
8 C. R. Bacon, P. K. Weber, K. A. Larsen, R. Reisenbichler, J. A. Fitzpatrick and J. L. Wooden, *Can. J. Fish. Aquat. Sci.*, 2004, **61**, 2425–2439.
9 Y. Amano, M. Kuwahara, T. Takahashi, K. Shirai, K. Yamane, H. Amakawa and T. Otake, *Aquat. Biol.*, 2013, **19**, 85–95.
10 C. C. Muhlfeld, B. Marotz, S. R. Thorrold and J. L. FitzGerald, *Trans. Am. Fish. Soc.*, 2005, **134**, 945–959.
11 M. Trudel, B. D. Walther and S. R. Thorrold, *Can. J. Fish. Aquat. Sci.*, 2010, **67**, 1699–1707.
12 A. Zitek, J. Irrgeher, A. Jagsch, M. Kletzl, T. Weismann and T. Prohaska, *Fish. Manag. Ecol.*, 2013, **20**(4), 354–361.
13 R. R. Warner, S. E. Swearer, J. E. Caselle, M. Sheehy and G. Paradis, *Limnol. Oceanogr.*, 2005, **50**, 1529–1542.
14 S. R. Thorrold, G. P. Jones, S. Planes and J. A. Hare, *Can. J. Fish. Aquat. Sci.*, 2006, **63**, 1193–1197.
15 H.-L. Yuan, S. Gao, M.-N. Dai, C.-L. Zong, D. Günther, G. H. Fontaine, X.-M. Liu and C. Diwu, *Chem. Geol.*, 2008, **247**, 100–118.
16 A. R. Kylander-Clark, B. R. Hacker and J. M. Cottle, *Chem. Geol.*, 2013, **345**, 99–112.
17 C. M. Fisher, J. D. Vervoort and S. A. DuFrane, *Geochem., Geophys., Geosyst.*, 2014, **15**, 121–139.
18 C. Huang, Y.-H. Yang, J.-H. Yang and L.-W. Xie, *J. Anal. At. Spectrom.*, 2015, **30**, 994–1000.
19 D. J. Goudie, C. M. Fisher, J. M. Hanchar, J. L. Crowley and J. C. Ayers, *Geochem., Geophys., Geosyst.*, 2014, **15**(6), 2575–2600.
20 C. A. Wehe, A. Ä. Niehoff, G. M. Thyssen, M. Sperling and U. Karst, *Rapid Commun. Mass Spectrom.*, 2014, **28**, 2627–2635.
21 B. R. Hacker, A. R. C. Kylander-Clark, R. Holder, T. B. Andersen, E. M. Peterman, E. O. Walsh and J. K. Munnikhuis, *Chem. Geol.*, 2015, **409**, 28–41.
22 D. R. Viete, A. R. C. Kylander-Clark and B. R. Hacker, *Chem. Geol.*, 2015, **415**, 70–86.
23 M. Aramendia, L. Rello, S. Bérail, A. Donnard, C. Pecheyran and M. Resano, *J. Anal. At. Spectrom.*, 2015, **30**, 296–309.
24 A. Zitek, J. Aléon and T. Prohaska, in *Sector Field Mass Spectrometry for Elemental and Isotopic Analysis*, ed. T. Prohaska, J. Irrgeher, A. Zitek and N. Jakubowski, Royal Society of Chemistry, Oxfordshire, 2014, DOI: 10.1039/9781849735407-00152, ch. 9, pp. 152–182.
25 J. Draxler, A. Zitek, M. Meischel, S. E. Stranzl-Tschegg, B. Mingler, E. Martinelli, A. M. Weinberg and T. Prohaska, *J. Anal. At. Spectrom.*, 2015, **30**, 2459–2468.
26 A. Zitek, J. Irrgeher, M. Cervicek, M. Horsky, M. Kletzl, T. Weismann and T. Prohaska, *Mar. Freshwater Res.*, 2014, **65**, 978–986.
27 L. Anselin, *Geographical Analysis*, 1995, vol. 27, pp. 93–115.
28 A. Mitchell, *The ESRI Guide to GIS Analysis: Spatial Measurements and Statistics*, 2005, vol. 2, p. 252.
29 SPSS, *The SPSS TwoStep Cluster Component: A Scalable Component Enabling More Efficient Customer Segmentation*, White Paper - Technical Report, Chicago, 2001.
30 B. Paul, C. Paton, A. Norris, J. Woodhead, J. Hellstrom, J. Hergt and A. Greig, *J. Anal. At. Spectrom.*, 2012, **27**, 700–706.
31 C. Paton, J. Hellstrom, B. Paul, J. Woodhead and J. Hergt, *J. Anal. At. Spectrom.*, 2011, **26**, 2508–2518.
32 M. Vihtakari, Measure growth patterns and align sampling spots in photographs: sclero tutorial, https://cran.r-project.org/web/packages/sclero/vignettes/sclero_tutorial.pdf, last access at 14.5.2016.
33 A. Zitek, M. Sturm, H. Waidbacher and T. Prohaska, *Fish. Manag. Ecol.*, 2010, **17**, 435–445.
34 B. M. Pracheil, J. D. Hogan, J. Lyons and P. B. McIntyre, *Fisheries*, 2014, **39**, 451–465.
35 C. C. Muhlfeld, S. R. Thorrold, T. E. McMahon and B. Marotz, *Can. J. Fish. Aquat. Sci.*, 2012, **69**, 906–915.